

A FFT-accelerated multi-block finite-difference solver for massively parallel simulations of incompressible flows^{*}

Pedro Costa^a

^a*Faculty of Mechanical, Industrial Engineering, and Computer Science, University of Iceland, Hjarðarhagi 2-6, 107 Reykjavik, Iceland*

Abstract

We present a multi-block finite-difference solver for massively parallel Direct Numerical Simulations (DNS) of incompressible flows. The algorithm combines versatility of a multi-block solver with the method of eigenfunctions expansions, to speedup the solution of the pressure Poisson equation. This is achieved by employing FFT-based transforms along one homogeneous direction, which effectively reduce the problem complexity at a low cost. These FFT-based expansions are implemented in a framework that unifies all valid combinations of boundary conditions for this type of method. Subsequently, a geometric multigrid solver is employed to solve the reduced Poisson equation in a multi-block geometry. Particular care was taken here, to guarantee the parallel performance of the multigrid solver when solving the reduced linear systems equations. We have validated the overall numerical algorithm and assessed its performance. The results show that 4 – 8-fold reduction in computational cost may be easily achieved, if the number of grid cells along the homogeneous direction is large enough. The solver, *SNaC*, has been made freely available and open-source under the terms of a MIT license.

Keywords: Computational Fluid Dynamics, Direct Numerical Simulation, High-Performance Computing, Fast Poisson Solver, Multi-Block Solver

1. Introduction

Incompressible fluid flows abound in the nature and industry. From the nanoliter scales of the flow through capillary blood vessels, to the atmosphere dynamics at the planetary scale, there is a kaleidoscope of important phenomena with fluid dynamics in the leading role. Moreover, most fluid flows beyond the centimeter scale are in the turbulent state, exhibiting complex three-dimensional, chaotic dynamics that span a vast spectrum of scales. Indeed, this complexity has challenged generations of physicists and engineers to bridge the gap between our limited understanding of turbulent flows, and their prevalent nature. One of the main challenges stems from the nature of the Navier-Stokes equations governing fluid flows, which are highly non-linear, making its analysis extremely difficult.

Fortunately, the continuous developments of efficient numerical methods, together with the ever-increasing computing power [1], enabled a paradigm-changing tool in fluid dynamics research: the Direct Numerical Simulations

^{*}Source code open and available under the terms of a MIT License on github.com/p-costa/SNaC.

Email address: pcosta@hi.is (Pedro Costa)

(DNS) of the Navier-Stokes equations. A DNS resolves all the scales of a fluid flow, providing a unique three-dimensional and time-resolved insight into their dynamics. Tremendous developments have followed the first DNS of homogeneous isotropic turbulence by Orszag and Patterson Jr [2] in 1972, being now possible to simulate canonical flows with trillions of spatial degrees of freedom [3, 4].

Finite-difference methods have been widely used in DNS of incompressible turbulent flows, particularly second-order, explicit finite-difference methods, following the seminal works of Kim and Moin [5], Verzicco and Orlandi [6]. Being typically very efficient, these methods can reproduce important observables in canonical fluid flows with the same fidelity as spectral methods [7, 8], while being more versatile in terms of the types of geometries and boundary conditions that can be treated, and the incorporation of more complex phenomena. Indeed, combined with immersed-boundary methods to simulate the flow over complex geometries [9, 10, 11], interface-tracking/-capturing methods for multi-fluid flows [12, 13], or to simulate canonical flows at very high Reynolds numbers [4], finite-difference methods have been playing a major role in DNS.

The incompressible Navier-Stokes equations have a highly non-local nature, due to the need to couple a constraint of zero velocity divergence – mass conservation – to the momentum transport equation. This typically involves a solution of a Poisson equation for a pressure field, which is used to project the velocity field into a divergence-free space [14]. The Poisson equation encapsulates the main challenge of solving the incompressible Navier-Stokes equations in a massively parallel framework – any disturbance in the system is propagated instantly and everywhere by the pressure. Indeed, the Poisson solver is typically the most expensive and elaborate part of an incompressible DNS solver.

Geometric multigrid methods have been proving to be efficient in solving the second-order finite-difference Poisson equation [15]. These methods exhibit excellent scaling properties, allow for non-uniform grids, and are versatile in the boundary conditions that can be accommodated. In relatively simple domains, however, very efficient direct solvers can be used instead, e.g. by exploiting the method of eigenfunctions expansions [16, 17]. This method uses Fourier-based expansions which reduce the number of diagonals of the linear system in two domain directions, resulting in a simple tridiagonal system which can be efficiently solved with Gauss elimination [18]. Thanks to the continuous improvements of frameworks for development of parallel algorithms, this approach has regained popularity and has been employed in numerous recent studies [19]. Indeed, this method has allowed for breakthroughs in e.g. DNS of single-phase canonical turbulent flows [20, 4], in complex geometries by using immersed-boundary methods [10], and in multi-phase flows [21, 22, 23], with at least two open-source DNS codes, *AFiD* [24] and *CaNS* [19], leveraging this approach. Despite most works in the literature only exploiting the method of eigenfunctions expansions along periodic directions [25], these Fourier-based expansions may be actually employed for many different combinations of boundary conditions [17].

To our best knowledge, finite-difference numerical algorithms reported in the literature using FFT-based finite-difference solvers are restricted to very simple geometries such as a rectangular box [26, 19] or cylindrical/spherical domains [24, 27], which may be extended to handle more complex geometries using immersed-boundary methods

[28]. Despite their proven fidelity to treat complex geometries efficiently, single-box solvers with immersed-boundary methods are not adequate for cases where a substantial portion of the computational domain is masked by the immersed solid volume (e.g., a narrow T-junction type of geometry), due to a large number of superfluous calculations outside the physical domain. These type of geometries are better suited for a solver that can be partitioned into multiple boxes, or *blocks*, to solve the Navier-Stokes equations only in the relevant physical domain.

The present work aims precisely to relax the restriction of current high-fidelity finite-difference DNS solvers, while retaining the versatility and efficiency of FFT-based synthesis of the Poisson equation. To this goal, we present an efficient multi-block Navier-Stokes solver for massively parallel simulations of fluid flows. The solver may leverage the method of eigenfunctions expansions to solve the Poisson equation along one homogeneous ‘*extruded*’ direction, decoupling the systems of equations in that direction, and employs highly efficient geometric multigrid solvers [29] for the reduced systems of equations. Similarly to the DNS code *CaNS*, the FFT-based expansion is implemented so as to cover all valid combinations of boundary conditions. The resulting tool, *SNaC*, has been made freely available and open-source.

We present the design and implementation of the algorithm in a massively parallel framework, with adaptations to leverage *HYPRE* library of multigrid solvers to solve the reduced Poisson equation after FFT-based synthesis. The results illustrate the high efficiency and versatility of this approach in different systems, especially in cases where the number of points along the direction of FFT-based reduction is high, resulting in up to a 8-fold speedup of the numerical calculation. Hence, in the same spirit as efficient single-block codes such as *CaNS* and *AFiD*, *SNaC* serves as a good base multi-block DNS solver, on top of which extensions to handle more complex physics such as two-phase flows or irregular geometries can also be implemented.

Next, in Section 2, we will describe the governing equations and numerical method. Then Section 3 presents our general implementation strategy, and the approach to enable simulations in a massively parallel setting. We will then present in Section 4 the validation of the numerical algorithm, and assess its performance. Finally, Section 5 provides a summary and future perspectives.

2. Governing Equations and Numerical Method

The numerical algorithm solves the incompressible Navier-Stokes equations for a fluid with unit density $\rho = 1$ and kinematic viscosity ν ,

$$\nabla \cdot \mathbf{u} = 0, \tag{1}$$

$$\frac{\partial \mathbf{u}}{\partial t} + \nabla \cdot (\mathbf{u} \otimes \mathbf{u}) = -\nabla p + \nu \nabla^2 \mathbf{u}, \tag{2}$$

with \mathbf{u} and p being the fluid velocity vector and pressure.

These equations discretized in a structured Cartesian grid with staggered velocity cells, using a second-order finite-difference/finite-volume method [30], integrated in time using a low-storage three-step Runge-Kutta scheme (RK3) in

a standard fractional-step method [14, 5, 31]. The grid spacing may vary along at least two of the domain directions, depending on the approach employed for solving the Poisson equation. The time advancement is fully explicit, and reads at each substep k ($k = 1, 2, 3$; $k = 1$ corresponds to a time level n and $k = 3$ to $n + 1$):

$$\mathbf{u}^* = \mathbf{u}^k + \Delta t (\alpha_k (\mathcal{A}\mathbf{u}^k + \nu \mathcal{L}\mathbf{u}^k) + \beta_k (\mathcal{A}\mathbf{u}^{k-1} + \nu \mathcal{L}\mathbf{u}^{k-1}) - \gamma_k \mathcal{G}p^{k-1/2}), \quad (3)$$

$$\mathcal{L}\Phi = \frac{\mathcal{D}\mathbf{u}^*}{\gamma_k \Delta t}, \quad (4)$$

$$\mathbf{u}^k = \mathbf{u}^* - \gamma_k \Delta t \mathcal{G}\Phi, \quad (5)$$

$$p^{k+1/2} = p^{k-1/2} + \Phi, \quad (6)$$

where \mathcal{A} , \mathcal{L} , \mathcal{G} , and \mathcal{D} denote the discrete advection, Laplacian, gradient and divergence operators; \mathbf{u}^* is the prediction velocity and Φ the correction pressure. The RK3 coefficients are given by $\alpha = \{8/15, 5/12, 3/4\}$, $\beta = \{0, -17/60, -5/12\}$, and $\gamma = \alpha + \beta$. A sufficient criterion for a stable temporal integration is given in [32]:

$$\Delta t \leq \min \left(\frac{1.65 \Delta \ell^2}{\nu}, \frac{\sqrt{3} \Delta \ell}{\max \|\mathbf{u}\|_1} \right), \quad (7)$$

with $\|\mathbf{u}\|_1$ the ℓ_1 -norm of \mathbf{u} , and $\Delta \ell$ the smallest grid spacing. Optionally, the temporal integration of the diffusion term may be treated implicitly. To achieve that, we directly solve three additional Helmholtz equations using the same numerical method that is used for the Poisson equation, even though a more efficient alternating diagonal implicit (ADI) approach could also be employed [33, 5].

Poisson Solver

One essential feature of the present method concerns the solution of the Poisson equation for the correction pressure Φ . The equation at grid point i, j, k reads, assuming constant grid spacing in each direction for simplicity,

$$\begin{aligned} & (\Phi_{i-1,j,k} - 2\Phi_{i,j,k} + \Phi_{i+1,j,k})/\Delta x_1^2 + \\ & (\Phi_{i,j-1,k} - 2\Phi_{i,j,k} + \Phi_{i,j+1,k})/\Delta x_2^2 + \\ & (\Phi_{i,j,k-1} - 2\Phi_{i,j,k} + \Phi_{i,j,k+1})/\Delta x_3^2 = f_{i,j,k}, \end{aligned} \quad (8)$$

which corresponds to a linear system represented by a Poisson matrix with 7 non-zero diagonals; Δx_m denotes the grid spacing in direction x_m ($m = 1, 2$, or 3). Here we exploit the method of eigenfunctions expansions to reduce the complexity of the Poisson equation by decoupling it along one direction, say x_2 . To achieve this *Fourier synthesis* [17], a Fourier-based discrete expansion operator, \mathcal{F}_{x_m} , is employed to Eq. (8), resulting in the following Helmholtz equation,

$$-\left(\frac{2}{\Delta x_1^2} + \frac{2}{\Delta x_3^2} - \frac{\lambda_j}{\Delta x_2^2} \right) \hat{\Phi}_{i,j,k} + \frac{\hat{\Phi}_{i-1,j,k} + \hat{\Phi}_{i+1,j,k}}{\Delta x_1^2} + \frac{\hat{\Phi}_{i,j,k-1} + \hat{\Phi}_{i,j,k+1}}{\Delta x_3^2} = \hat{f}_{i,j,k}, \quad (9)$$

where $\hat{\square} = \mathcal{F}_{x_m}(\square)$, denotes the Fourier-based discrete transform along direction x_m , and λ_m is an eigenvalue. The eigenfunction expansion \mathcal{F}_{x_m} and eigenvalue λ_m depend on the boundary conditions at each end of the expansion direction, which have to be satisfied by the corresponding inverse operator $\mathcal{F}_{x_m}^{-1}$. For instance, \mathcal{F}_{x_m} would be the discrete Fourier transform in case of periodic boundary conditions, or a discrete sine transform in case of Dirichlet boundary conditions at both ends. Indeed, various eigenfunction expansions and eigenvalues for different combinations of boundary conditions may be employed. The types of direct and inverse discrete transforms \mathcal{F}_{x_m} and corresponding eigenvalues λ_m for different combinations of (staggered) boundary conditions are listed in Table 1, and we refer to e.g. [17, 34, 19] for more details.

Table 1: Eigenvalues, and forward (\mathcal{F}) and backward (\mathcal{F}^{-1} , multiplied by the normalization factor $n\theta$) transforms for different combinations of (staggered) boundary conditions. The eigenvalues in Eq. (9) are given by $\lambda_m = -4 \sin^2(\pi l_m/n)$, $m = 0, \dots, n-1$ [17], with n being an even number of grid cells in the direction of synthesis. The mathematical expressions for the different transforms can be found in e.g. [19]. Here (I)DFT denotes the (inverse) discrete Fourier transform, and DST/DCT the different standard types of discrete sine/cosine transforms.

Boundary Conditions	$l_q (\lambda_q = -4 \sin^2(\pi l_q/n))$	\mathcal{F}	$n\theta \mathcal{F}^{-1}$	θ
Periodic	$q+1$	DFT	IDFT	1
Neumann–Neumann	$q/2$	DCT-II	DCT-III	2
Dirichlet–Dirichlet	$(q+1)/2$	DST-II	DST-III	2
Neumann–Dirichlet	$(2q+1)/4$	DCT-IV	DCT-IV	2

The advantage of this Fourier synthesis of Eq. (8) is that all discrete transforms presented in Table 1 may exploit the FFT algorithm, resulting in a relatively low cost of $O(N \log n_2)$ operations, with N the total number of grid points, and n_2 the number of grid points along x_2 . Note, however, that the grid is required to be uniform in the direction of synthesis.

In simple rectangular boxes, it is beneficial to further simplify this equation by employing this Fourier synthesis in a second direction, say in x_3 . With a total cost of $O(N \log n_2 n_3)$ operations [19], the two reductions enable an efficient, *direct* solution of the Poisson equation – the problem is simplified to the solution of $n_2 n_3$ tridiagonal systems with n_1 unknowns ($O(n_1 n_2 n_3) = O(N)$ operations). This was the approach used in the DNS solver *CaNS* [19], and showed excellent performance. In a multi-block domain, instead, the geometry is expected to be more complex, with the number of grid points n_1 and n_2 varying among blocks. This makes a two-dimensional FFT-based synthesis impractical to implement in a distributed-memory framework. Even so, employing this synthesis in one direction to obtain Eq. (9) is often possible and desirable – there are numerous interesting cases where a multi-block, two-dimensional configuration that is ‘extruded’ in a third direction, such as a T-junction, a cross-slot, a square elbow type of geometry. These are precisely the type of geometries, homogeneous along one direction, which can benefit from FFT-acceleration of the Poisson equation in the present method.

It is interesting to note that the computational complexity of efficient iterative methods such as a geometric multi-grid solver for Eq. (8) scales with $O(N)$, while a direct solution with Fourier synthesis in two directions scales less efficiently, $O(N \log n_2 n_3)$. Interestingly, so far, FFT-based direct solvers of a Poisson equation, with $N \sim 10^9 - 10^{10}$ have been reported to yield excellent performance 3 – 10 times faster than well-established a geometric multigrid

solvers (depending on the type of solver and desired tolerance; see, e.g., [35]). While this trend is expected to reverse for sufficiently high values of N , the term $\log n_2 n_3$ grows slowly, meaning current ambitious problem sizes may still be orders-of-magnitude too small for efficient iterative methods to overperform direct FFT-based solvers.

In the absence of Fourier synthesis, Eq. (8) is solved using the efficient parallel semicoarsening multigrid solver PFMG (which uses a point-wise smoother), or the more robust SMG solver (which uses a plane smoother) [29], available in the *HYPRE* library.

When Fourier synthesis is employed, the same solvers are used to solve the resulting decoupled two-dimensional Poisson equations. It is important to note that the magnitude of the diagonal elements of the matrix corresponding to each two-dimensional system (Eq. (9)) will vary according to λ_j (c.f. Table 1). Hence, the iterative solution convergence is expected to vary among the two-dimensional systems [15], requiring a larger number of iterations for smaller values of λ_j .

For clarity, the steps undertaken to solve the Poisson equation in this case are described below, in Algorithm 1, for a square box with dimensions $n_1 \times n_2 \times n_3$ and Fourier synthesis along x_2 .

Algorithm 1 Summary of the steps required for solving Eq. (8) in a $n_1 \times n_2 \times n_3$ box, using Fourier synthesis along x_2 .

```

do  $i = 1$  to  $n_1$  and  $k = 1$  to  $n_3$  ▷  $O(n_1 n_3 \cdot n_2 \log n_2)$  operations
  forward FFT-based transform along  $x_2$  of right-hand-side of Eq. (8):  $\hat{f}_{i,1\dots n_2,k} = \mathcal{F}_{x_2}(f_{i,1\dots n_2,k})$ 
end do
do  $j = 1$  to  $n_2$  ▷  $O(n_2 \cdot n_1 n_3)$  operations.
  solve Eq. (9) using a geometric multigrid solver to obtain  $\hat{\Phi}_{1\dots n_1,j,1\dots n_3}$ 
end do
do  $i = 1$  to  $n_1$  and  $k = 1$  to  $n_3$  ▷  $O(n_1 n_3 \cdot n_2 \log n_2)$  operations
  backward FFT-based transform along  $x_2$  of the previous solution:  $\Phi_{i,1\dots n_2,k} = \mathcal{F}_{x_2}^{-1}(\hat{\Phi}_{i,1\dots n_2,k})$ 
end do

```

Important implementation details for solving these equations in a massively parallel paradigm will follow next.

3. Implementation Strategy

The numerical tool has been implemented in modern Fortran, and extended an MPI/OpenMP standard for distributed- and shared-memory parallelization. The OpenMP extension serves to guide future porting efforts to heterogeneous (e.g. many-GPU) systems, which may exploit directive-based approaches for thread-level parallelism; its performance will not be discussed here.

3.1. Computational setup

The problem is set by two kinds of computational parameters – *global* and *block-specific*. Global parameters are those common to all blocks, such as physical properties and reference scales, time step control, simulation stopping criteria and I/O frequency; block-specific parameters set, for each block, the geometry and computational mesh, the boundary conditions (including inter-block connectivity), and the three-dimensional block domain partitioning into

different computational subdomains, to be assigned to an MPI process. These parameters have to be set such that the grid along the boundaries of connected blocks is congruent, so the whole computational domain is discretized on a structured grid. Moreover, the partitioning into different computational subdomains is conditioned to the following rules:

- blocks can be decomposed in the three domain directions, and each MPI process is assigned *exclusively* to one of the corresponding computational subdomains. Consequently, each block needs to be assigned to at least one MPI process;
- each side of a computational subdomain is either a physical boundary, or is connected to a single neighboring subdomain;
- if FFT-based synthesis of the Poisson equation is used, the computational subdomains cannot be decomposed along the direction of synthesis (i.e., a pencil-like domain decomposition is required).

Fig. 1 presents an example of a valid computational setup in two dimensions, where the geometry is partitioned into 4 blocks and a total of 16 computational subdomains. As the figure illustrates, MPI ranks are grouped consecutively within each block, with row-major ordering. Those partitions are set by a block-specific input parameter dictating the number of subdivisions in each direction. The partitioning is then performed so as to distribute as evenly as possible the block grid cells among the different subdomains.

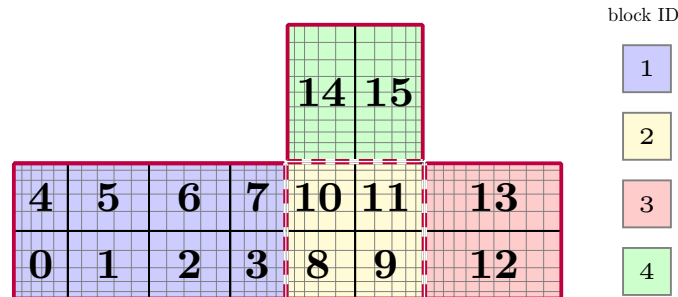


Figure 1: Illustration of a valid multi-block setup in two dimensions. The red solid lines denote physical boundaries, while the dashed lines denote internal boundaries. The four blocks (depicted in different colors) are partitioned into several computational subdomains (depicted by the different numbers). The non-uniform grid was obtained using hyperbolic tangent based mapping functions; see, e.g., [36, 37]. The computational parameters used to generate this grid are reported in Table 2, and described in its caption.

In practice, the blocks are defined as illustrated in Table 2 (corresponding to the setup in Fig. 1). First, the coordinates of the lower and uppermost corners of each block (l_o and h_i) are defined in index space, i.e., in a coordinate system with arbitrary origin and uniform spacing equal to 1, such that the number of grid points in each direction is equal to $h_i - l_o + 1$. Then the physical coordinates of each of the corners are defined by parameters l_{min} and l_{max} , and a mapping function of choice is used to determine the coordinates of the grid points in the physical coordinate system (e.g., to achieve a grid clustering bias). In Table 2, gr_type defines the mapping function type, and gr_factor is a parameter dictating the degree of clustering. Finally, $dims$ sets the number of partitions of the

block, in each direction. The caption of Table 2 explains in more detail how those parameters result in the configuration of Fig. 1. We should note that a two-dimensional system is naturally obtained from a three-dimensional setup using two grid cells and a small domain length along one direction, with a two-dimensional initial condition.

Table 2: Block-specific parameters for the two-dimensional configuration in Fig. 1. `lo` and `hi` are the index space coordinates of the lower and uppermost corners of each block in index space; `lmin` and `lmax` the physical coordinates of these corners; `gr. type` denotes the choice of grid mapping functions, which have to be congruent among blocks (among the family of functions implemented in *SNaC*, we used here hyperbolic tangent clustering at two ends (0), or just at the lower/upper end $-1/+1$); `gr. factor` is the grid stretching parameter of the mapping function, with 0.0 corresponding to a uniform mapping [36, 37]; `dims` dictates the MPI partitioning along each direction.

block ID	lo	hi	lmin	lmax	gr. type	gr. factor	dims
1	[1, 1, 1]	[40,10,2]	[0.,0.,0.]	[4.,1.,0.1]	[0, 0, 0]	[2.5,1.,0.]	[4,2,1]
2	[41, 1, 1]	[50,10,2]	[4.,0.,0.]	[1.,1.,0.1]	[-1,-1, 0]	[1.5,1.,0.]	[2,2,1]
3	[51, 1, 1]	[60,10,2]	[5.,0.,0.]	[1.,1.,0.1]	[1, 1, 0]	[1.5,1.,0.]	[1,2,1]
4	[41,11, 1]	[50,20,2]	[4.,1.,0.]	[5.,2.,0.1]	[0, 0, 0]	[2.5,1.,0.]	[2,1,1]

Finally, physical and block-block boundary conditions need also to be specified. Three kinds of boundary conditions may be set for the velocity and pressure – Dirichlet, Neumann, or block-block connectivity, with periodic boundary conditions being naturally set by a cyclic sequence of connectivity conditions along one direction. Naturally, the velocity and pressure boundary conditions need to be consistent, so that the pressure projection step at the boundary yields the expected normal velocity component (e.g., a prescribed velocity requires a zero normal gradient of Φ).

3.2. Overview of parallel implementation strategy

The following steps are performed to setup the calculation in a distributed-memory framework:

1. **Assign MPI tasks to the computational subdomains:** for each block, subsets of the total number of MPI processes (hereafter denoted `comm_world`) are assigned to each computational subdomain, and the corresponding local grid spacing and extents are determined as illustrated in the previous section;
2. **Determine neighboring MPI tasks:** for each computational subdomain, the tasks IDs of the eight neighboring subdomains (i.e., 2 per domain direction) are determined and stored (with `MPI_RANK_NULL` tagging a non-cyclic physical boundary);
3. **Describe data structures for boundary data exchange:** data structures for ghost cells communication among neighboring tasks are created (`MPI_TYPE_VECTOR` describing the boundary data layout), as well as a communicator `comm_block` grouping the tasks per block, to be used for post-processing and I/O.

Once these initialization steps are performed and the neighbors of each MPI process determined, *the algorithm becomes agnostic of the disposition of blocks* – communication of ghost cell data between neighboring computational subdomains (so-called halo exchange) may be performed with, e.g., a `MPI_SENDRECV` call, without discerning internal and external block boundaries.

Finally, MPI-I/O is used to write field data into a single binary file per block, which is accompanied by a file logging the saved data information. This allows visualizing field data as a time series using a simple XDMF metadata file [38].

3.3. Massively parallel Poisson solver

The different solution strategies for solving Eq. (8) on a multi-block geometry are described below¹. A common denominator in these approaches is the efficient and well established *HYPRE* library of high-performance multigrid solvers. Indeed, the library Structured-Grid-System (*Struct*) interface enabled a versatile implementation, however with excellent performance. It should be noted that the implementation allows for flexibility in the choice of the direction of FFT-based synthesis (or no synthesis at all) by employing (cpp) source pre-processing.

3.3.1. Geometric multigrid solver without FFT-based synthesis

Solving Eq. (8) without FFT-based synthesis is a canonical use case of the *HYPRE*'s *Struct* interface. In a nutshell, the interface defines a distributed coefficient matrix by passing to the library:

1. the MPI communicator where the calculation is to be performed (here `comm_world`);
2. the extent of each computational subdomain in index space (same convention as parameters `lo` and `hi` in Table 2);
3. information about the finite-difference stencil associated with the system;
4. the 7 non-zero elements of the coefficient matrix (one per stencil entry), for each grid point within the computational subdomain.

Subsequently, the setup of the right-hand-side and initial guess vectors, and the setup of the geometric multigrid solver are straightforward. These initialization steps are performed once in the beginning of the calculation², and the Poisson equation then solved every RK3 substep using the previous solution as the initial guess.

3.3.2. FFT-accelerated solution of the Poisson equation

The FFT-accelerated solution of the Poisson equation described in Algorithm 1 can be employed as long as the domain has one homogeneous ‘*extruded*’ direction with constant grid spacing. We adopted the implementation of FFT-based synthesis in *CaNS* [19], which uses the GURU interface of the *FFTW* library [39]. This approach computes all types of fast discrete transforms in Table 1 efficiently, in place, and with the same syntax, just by evoking the right transform type and considering the different scaling factors.

As illustrated in Algorithm 1, the first step is performing one-dimensional FFT-based transforms along the homogeneous direction, here taken as x_2 . To achieve this in a distributed memory paradigm, the domain is not decomposed

¹The implementation is actually more general, solving a Helmholtz equation on non-uniform Structured Cartesian grids, with staggered or non-staggered boundary conditions.

²If implicit temporal discretization of the diffusion term is used, not discussed here, the coefficient matrix diagonal needs to be modified at every RK3 substep, which is possible using *HYPRE*'s `HYPRE_StructMatrixAddToBoxValues`.

along x_2 , as illustrated in Fig. 2. In this *pencil* decomposition, each computational subdomain m has a size size $[n_1^m, n_2, n_3^m]$.

After employing the one-dimensional FFT-based transforms, n_2 *decoupled* 2D systems will be solved using the geometric multigrid method (recall Eq. (9)), with each system set analogously to the 3D system described above in Section 3.3.1. Using the pencil decomposition, these 2D linear systems can be solved consecutively, parallelized over `comm_world`, i.e., solving for $\hat{\Phi}_{1\dots n_1^m, j, 1\dots n_3^m}$, from $j = 1$ to n_2 . However, as we will see, solving such small linear systems in a massively parallel setting will result in a significant communication overhead, with all tasks synchronizing between each solve. Moreover, it is not yet possible to set explicitly a batch of systems to be solved collectively using the *HYPRE* library.

To circumvent this issue, we define batches of 2D systems as small 3D problems – 3D linear systems are set as previously described, but decoupled along x_2 by setting the stencil coefficients in this direction to zero. Care should be taken here, because the number of iterations to solve each 2D system varies along x_2 , due to the eigenvalue λ_{x_2} in the diagonal of each system (c.f. Eq. (9) and Table 1). If, for instance, a single distributed 3D matrix encapsulating the entire pencil subdomain with size $[n_1^m, n_2, n_3^m]$ is considered, much unnecessary work will be performed in the 3D problem, to match the maximum number of iterations of the slowest-converging 2D system. Hence, to cover the problem inhomogeneity along x_2 , the pencil subdomains are sliced into p chunks, hence with a size $[n_1^m, n_2^p, n_3^m]$ with $n_2^p = n_2/p$; see Fig. 2. The value of p is chosen so as to capture the inhomogeneity of the 2D systems, while retaining a balance between computation and communication³. The approach for the distributed FFT-accelerated Poisson equation is summarized in Algorithm 2.

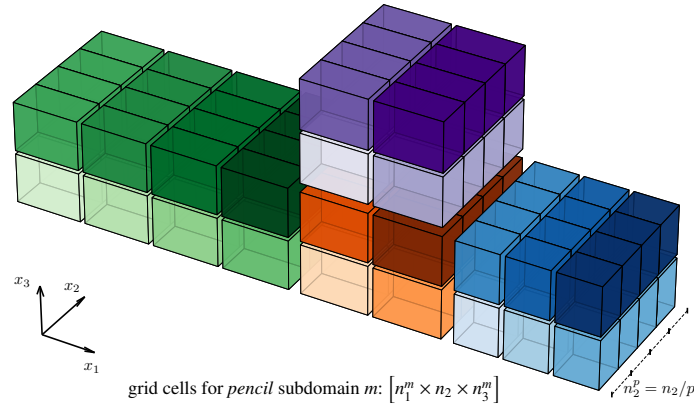


Figure 2: Illustration of the domain decompositions to solve the FFT-accelerated Poisson equation, assuming x_2 as the FFT synthesis direction. Different colors distinguish the tasks in different different blocks, while different lightness marks the MPI tasks within a block. After performing the FFT-based synthesis, to solve the resulting n_2 independent 2D linear systems, the pencils are partitioned by a factor p (here $p = 4$), and a 3D system decoupled along x_2 is defined for each chunk.

Finally, we devised an alternative approach to solve the decoupled 2D systems at the cost of one *all-to-all* collective operation. The approach follows the computation of the FFT-based transforms by a pencil–slab data redistribution,

³Note that the limiting case $p = 1$ leads to significant unnecessary work, and $p = n_2$ to large communication overheads.

Algorithm 2 Sequence of operations performed per task m for the parallel solution of the Poisson equation (Eq. (8)) with FFT-based synthesis, using ‘sliced pencils’; see Fig. 2.

```

do  $i = 1$  to  $n_1^m$  and  $k = 1$  to  $n_3^m$ 
  forward FFT-based transform along  $x_2$  of right-hand-side of Eq. (8):  $\hat{f}_{i,1\dots n_2,k} = \mathcal{F}_{x_2}(f_{i,1\dots n_2,k})$ 
end do
do  $J = 1$  to  $p$ 
  solve Eq. (9) in pencil chunk  $J$  within comm_world using a geometric multigrid solver, to obtain  $\hat{\Phi}_{1\dots n_1^m,(J-1)n_2^m+1\dots Jn_2^m,1\dots n_3^m}$ 
end do
do  $i = 1$  to  $n_1^m$  and  $k = 1$  to  $n_3^m$ 
  backward FFT-based transform along  $x_2$  of the solution:  $\Phi_{i,1\dots n_2,k} = \mathcal{F}_{x_2}^{-1}(\hat{\Phi}_{i,1\dots n_2,k})$ 
end do

```

allowing to solve the $2D$ systems explicitly, with balanced loads. For the sake of conciseness, this approach is described in [Appendix A](#).

4. Validation and Computational performance

4.1. Validation

Before presenting the validations of the numerical algorithm, we should note that verifying the implementation of the Poisson solver and pressure projection steps is simple, because the final velocity has to be divergence-free (up to the tolerance conditioned by the iterative error). This incompressibility condition is checked recurrently during the calculation.

Besides the different solution approach for the Poisson equation, the numerical method is equivalent to that of *CaNS*, which has been validated against several canonical turbulent flows (e.g. channel, square duct, and decaying Taylor-Green vortex) [19]. Hence, for simple rectangular boxes, all the validations shown in [19] for turbulent flows are easily reproduced by the present tool. We therefore restrict ourselves to computationally cheaper test cases in multi-block geometries. Unless otherwise stated, the simulations are integrated in time with a varying time step, $dt = CFL dt_{max}$, with dt_{max} the maximum allowed time step, and $CFL = 0.95$; the PFMG solver was seen to be efficient and robust enough for all cases, with tolerance and maximum number of iterations set to 10^{-4} and 50. Hereafter, u , v , and w will denote the x , y , and z components (x_1 , x_2 , and x_3 above) of the velocity.

Three-dimensional lid-driven cavity flow

We consider a three-dimensional lid-driven cavity flow, simulated in a cubic domain with dimensions $[-H/2, H/2]^3$. Zero velocity boundary conditions are prescribed at all the boundaries, except for the top wall, which moves with a velocity $u(x, H/2, z) = (U_L, 0, 0)$; the Reynolds number is $Re = U_L H / \nu = 1000$, and the flow is solved on a uniform grid with spacing $\Delta\ell = H/128$.

Fig. 3 shows the velocity profiles of the steady-state solution at the centerlines $u(0, y, 0)$ and $v(x, 0, 0)$, compared to the data extracted from [40], showing good agreement. It should be noted that the exact same setup was validated in [19], and the present results match that data with a maximum relative difference of 10^{-7} . We have also confirmed

that partitioning the geometry into smaller individual blocks (e.g. eight, two per domain direction) results in the exact same calculation.

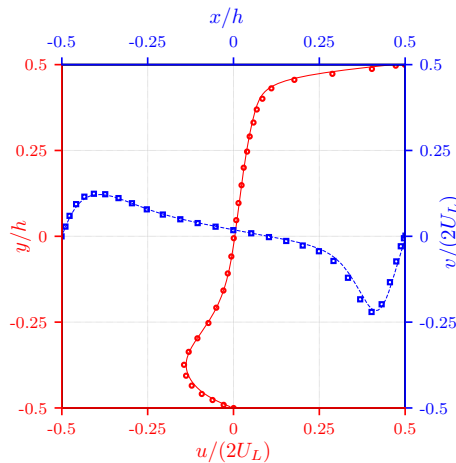


Figure 3: Normal velocity profiles along the centerlines $u(0, y, 0)$ and $v(x, 0, 0)$ for a lid-driven cubic cavity at $Re = 1000$. The symbols correspond to the data extracted from [40].

Laminar flow through a T-junction

We simulated the laminar T-junction flow shown in Fig. 4, with a constant channel height H , and composed of a short inlet branch, and two longer outlet branches, a geometry which requires at least four distinct blocks (c.f. Fig. 1). A fully developed Poiseuille profile is prescribed at the inlet, corresponding to a flow rate per unit depth \dot{Q} . At the outlet, the same profiles are prescribed, but for an exiting flow rate of $\chi\dot{Q}$ in the branching (vertical) channel, and $(1 - \chi)\dot{Q}$ in the main (horizontal) channel, with $\chi = 0.44$; no-slip and no-penetration boundary conditions are prescribed at the walls. The flow is governed by a Reynolds number $Re = \dot{Q}H^2/\nu = 248$, and is solved on a regular grid with constant spacing, $\Delta\ell = H/64$. The steady-state solution is depicted in Fig. 4, showing the velocity magnitude.

This setup was studied numerically for Newtonian and non-Newtonian fluids in Ref. [41], to reproduce the experiments in Ref. [42]. The shape and extent of the two recirculation regions at the entrance of each branch agree with what is reported in these references. More quantitatively, Fig. 5 shows the profiles of streamwise velocity in the main branch and derivative branches, at different cross sections, compared to the reference data extracted from [41]. The agreement is excellent.

4.2. Computational performance

We now assess the performance of the numerical algorithm in massively parallel calculations, with the different approaches for solving the Poisson equation. Three different setups are considered, with geometries defined by an increasing number of blocks: a lid-driven cavity flow (1 block), an L-shaped duct (3 blocks), the flow around a square

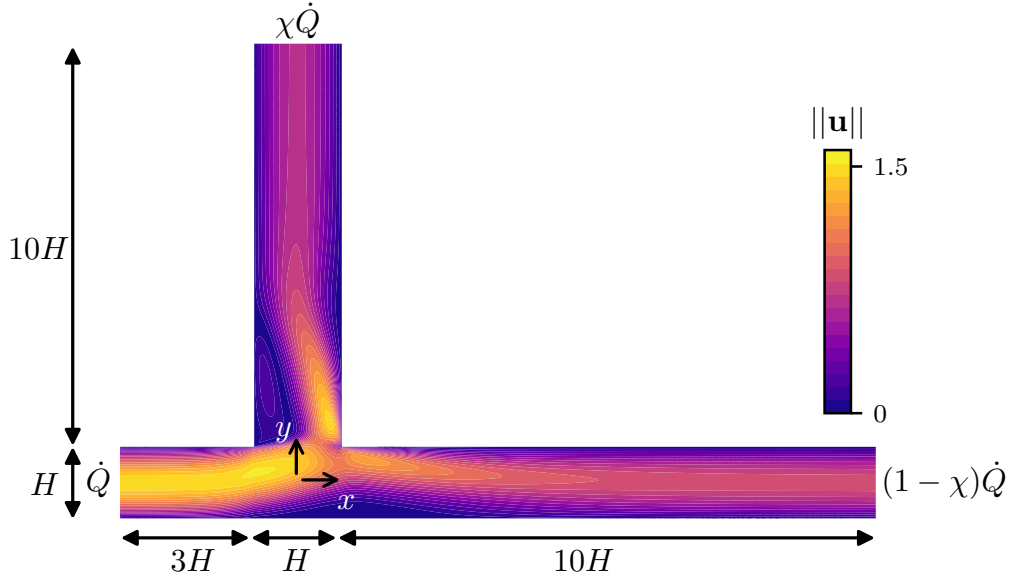


Figure 4: Schematic of the configuration for the T-junction simulation, with the contours of the steady-state velocity magnitude. A fully-developed Poiseuille profiles are prescribed with a flow rate \dot{Q} (inlet), $(1 - \chi)\dot{Q}$ (main branch outlet), and $\chi\dot{Q}$ (derivative branch outlet). Note that the height of the channel was increased for clarity.

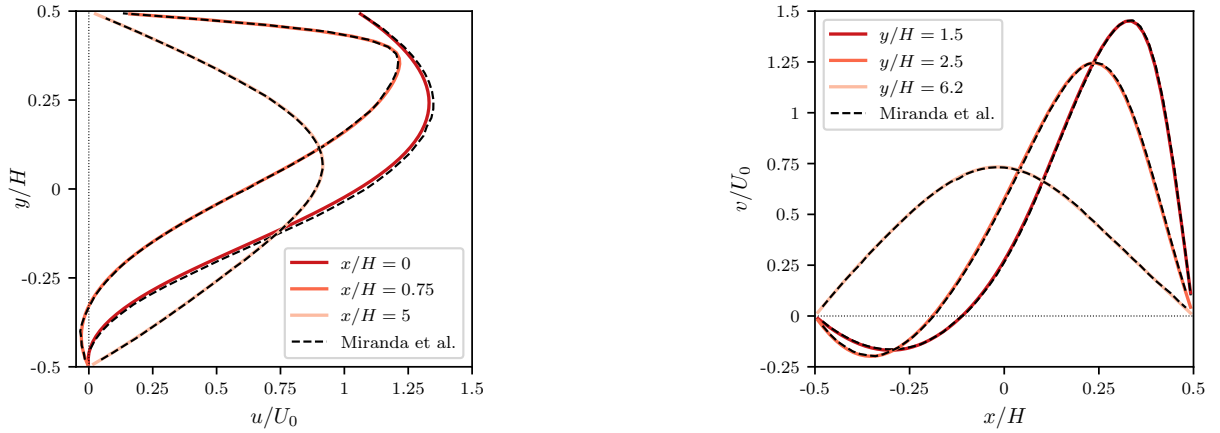


Figure 5: Profiles of streamwise velocity in the main branch (left) (x component, u), and derivative branch (right) (y component, v) of a T-junction, compared to the reference data in [41]. $U_0 = \dot{Q}H$ is the inlet bulk velocity.

obstacle (8 blocks). The lid-driven cavity flow corresponds to the problem described in Section 4.1; the other two cases are illustrated in Fig. 6, where the block partitioning can be also appreciated, and the computational parameters are described in the figure caption. Note that the L-channel is a clear example of a system better suited for a multi-block solver than a single-block DNS solver extended with an immersed-boundary method. Conversely, the flow around a square setup is more suited for leveraging such a single-block approach (see [43]), because it can be represented by a rectangular box with only a small portion of the domain – the square obstacle – excluded.

The timing measurements reported here correspond to the wall-clock time required to perform a full solution time

step (i.e., three RK3 substeps), averaged over 100 instances. The runs were performed on the supercomputer Tetralith based in Sweden (Xeon Gold 6130 16C 2.1GHz, Intel Omni-Path), with *SNaC* built using the Intel programming environment (18.0.1) with `-O3 -xHost -fp-model-fast` as optimization flags. It should be noted that solving the Poisson equation takes roughly 85 – 95% of the overall solution time, depending on the approach. For all the cases here, a pencil partitioning $p = 16$ (recall Algorithm 2) will be used, as it was found to result in a good scaling performance.

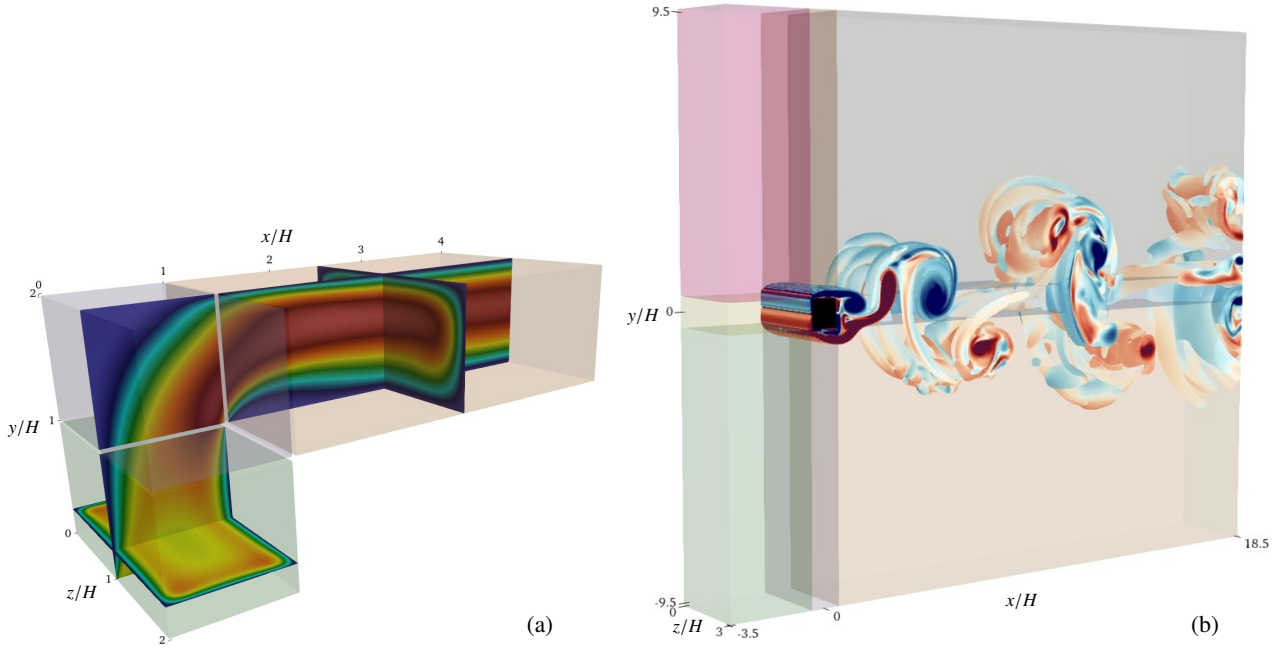


Figure 6: Multi-block computational setups considered in the scaling performance assessment, with the domain dimensions and the blocks depicted in different translucent colors. (a): flow in a L-shaped rectangular duct with height H , solved on a constant grid with $H/\Delta\ell = 256$. No-slip boundary conditions are prescribed everywhere, except at the inflow (bottom, with uniform velocity U), and at the outflow (zero pressure); the Reynolds number is $Re = UH/\nu = 500$. The planar contours show the steady-state velocity magnitude (red – high; blue – low). (b): turbulent flow around a square cylinder with size H solved on a constant grid with $H/\Delta\ell = 64$. The flow is periodic along the z direction, and a uniform velocity U is prescribed at the inflow, with zero pressure boundary conditions prescribed elsewhere for simplicity; the Reynolds number is $Re = 500$. The figure shows the regions of the domain with vorticity $|\omega| > 5U_b/H$, colored by the local spanwise vorticity ω_z in a divergent linear colormap (blue to red) clamped at $\omega_z = \pm 3$. For the scaling tests, the size of the top, bottom, and right blocks was halved, so to allow assessing scaling over a range of $O(10) - O(1000)$ cores.

Fig. 7(a) shows the strong scaling performance of the single-block case (lid-driven cavity) for two different grids (with $N = 512^3$ and 1024^3), with different directions of FFT synthesis. Clearly, the differences in performance for the different pencil orientations are small, with x -aligned pencils performing best due to a more favorable memory-access pattern. Interestingly, when FFT synthesis is used, the timings are much less sensitive to the pencil orientation. As expected from the excellent performance of the *HYPRE* library, the geometric multigrid solver without FFT acceleration scales very well, as it can be also depicted in the compensated plot in panel (b) of Fig. 7. Note that, there, the slight offset between cases with 512^3 and 1024^3 are due to a slightly larger number of iterations required for the iterative solver on the finer grid.

Somewhat expectedly, the FFT-accelerated approaches perform well for a small number of cores, showing a remarkable 2-fold speedup compared to the standard 3D multigrid solution. However, when increasing the number of cores, the importance of solving several 2D systems in parallel becomes evident. While the scaling quickly degrades when the 2D linear systems are solved naively in the pencil decomposition, it remains excellent with the other two approaches: when the slab-decomposed solution is used (Algorithm 3) the figure shows a consistent 2-fold speedup, until the maximum partitioning is reached; using the sliced-pencils approach in Algorithm 2 shows similar performance, but allows to reach a higher number of cores, until the load per task becomes too small and the scaling deteriorates. This occurs for a number of cores N_{CPU} larger than 1024 for the 512^3 setup, and larger than 2048 for the 1024^3 case. Nevertheless, the wall-clock time per step in the scaling region is already quite small.

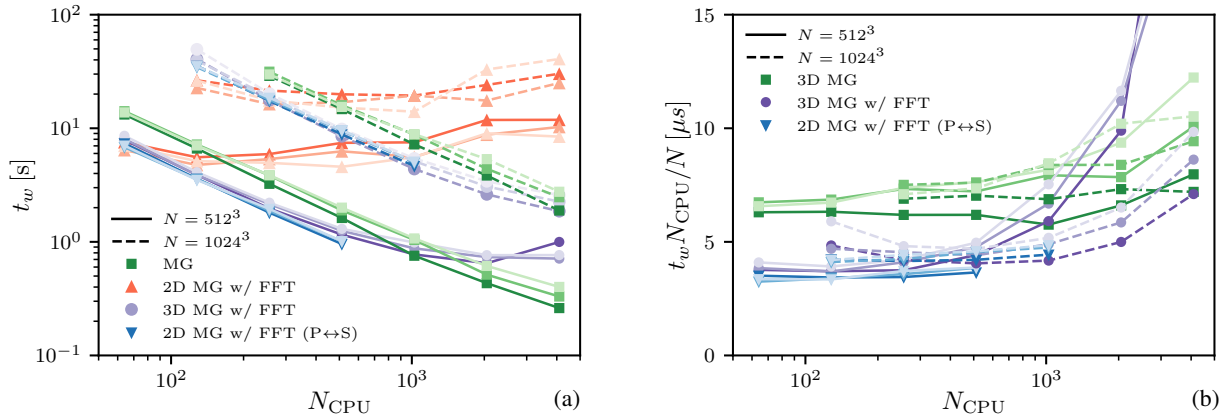


Figure 7: (a): strong scaling of the numerical algorithm up to 4096 cores, for a lid-driven cavity flow with 512^3 and 1024^3 grid cells, with different directions of FFT-based synthesis (x -, y -, or z -oriented by increasing color lightness). t_w denotes wall-clock time in seconds/time step/task (i.e. three Runge-Kutta substeps), and N_{CPU} the number of cores. ‘3D MG’ denotes the 3D multigrid solution, ‘2D MG w/ FFT’ the naive FFT-accelerated solution with 2D multigrid solution on a pencil domain decomposition, ‘3D MG w/ FFT’ the FFT-accelerated solution using 3D sliced pencils (Algorithm 2), and ‘MG w/ FFT P↔S’ the FFT-accelerated solution but with pencil–slab data redistribution (Algorithm 3). (b): compensated scaling plot showing the total CPU time per grid cell, per time step, with N being the total number of grid cells. Here a horizontal line corresponds to ideal scaling.

Fig. 8 shows the strong scaling performance of the other two cases considered, with a z -aligned pencil decomposition, and two different values of n_z while keeping the number of points in the other directions fixed; the domain length along z was also increased to keep the grid spacing constant. Here the blocks were decomposed among MPI tasks with a constant number of grid points per computational subdomain, to ensure load balancing. Remarkably, FFT-based acceleration results in a tremendous speedup for the L-channel case, with an almost 8-fold speedup compared to the standard iterative solution. Here, for the smaller value of $n_z = 256$ the sliced-pencils approach in Algorithm 2 performs best. Conversely, with larger values of n_z the overhead of the *all-to-all* collective in the slab-decomposed approach (Algorithm 3) becomes less significant, and the two approaches show very similar performance. Despite these differences, both approaches show a remarkable speedup, allowing for very small values of wall-clock time per step. Conversely, for the flow around the square case, the performance of the FFT-accelerated solver is less impressive, because the value of n_z relative to the problem size is smaller. Nevertheless, for larger n_z , up to about 5-fold speedup

can be observed. Here the communication overhead of the slab decomposed solver is too large, resulting in relatively poor performance. Still, despite the reasonable performance here for a smaller number of cores, we recall that this case is more suited for a simpler, single-block solution extended with an immersed-boundary method.

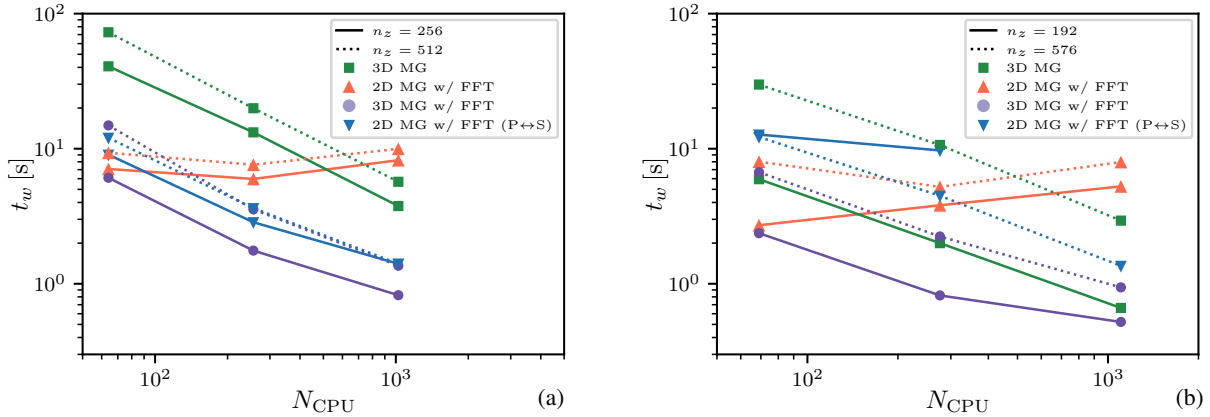


Figure 8: Strong scaling of the numerical algorithm for the L-channel case (a), and flow around a square case (b). The different approaches are considered, using z as the direction of FFT synthesis, for two different values of the number of grid points n_z . See the caption of Fig. 7 for the description of the cases in the legend.

To get a better impression of the performance gains for these three different canonical systems, Fig. 9 summarizes the increase in wall-clock time per step of the FFT-accelerated calculation, relative to the standard iterative solution. Clearly, the method performs best when the number of points in the direction of FFT synthesis is larger, which ensures a substantial load per task. Nonetheless, the results demonstrate the potential of this approach to speedup a multi-block DNS by large factors, and with small enough wall-clock time per time step.

5. Summary and Outlook

We have presented and validated a fast and versatile multi-block finite-difference solver for the incompressible Navier-Stokes equations. If the physical problem features one homogeneous direction, which is the case in numerous setups of interest, the numerical algorithm can exploit the method of eigenfunctions to decouple the finite-difference Poisson equation along that direction. This ‘synthesis’ of the Poisson equation can be employed at a very low cost using FFT-based transforms, and enables major gains in the performance of the overall numerical algorithm. We have implemented the different FFT-based expansions in a unified framework, to support all the valid combinations of boundary conditions of the method.

Following the FFT-based synthesis, a series of two-dimensional Poisson problems are solved using an efficient geometric multigrid solver. Here we leveraged the well established *HYPRE* library, which enables a flexible multi-block implementation, however with excellent performance. We have demonstrated that the most straightforward application of the library to this problem is bound to show poor parallel performance, and proposed two distinct strategies to improve the parallel scalability of the overall method. Both strategies were shown to greatly improve the

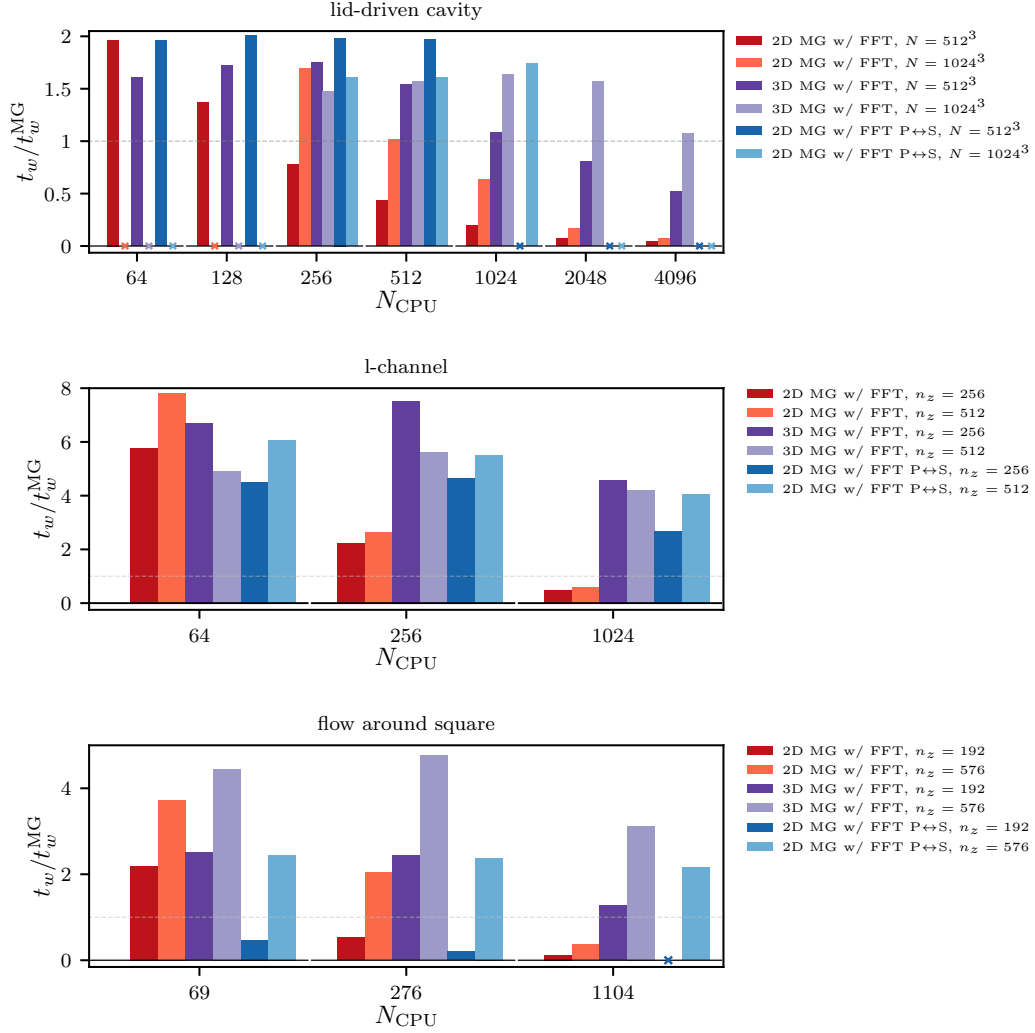


Figure 9: Speedup of the FFT-accelerated calculation with respect to the standard multigrid solution (with wall-clock time per step t_w^{MG}), as a function of the number of cores N_{CPU} , for the different cases considered, with z is taken as the FFT synthesis direction. The grey dashed line marks the threshold of performance gain $t_w = t_w^{MG}$, and the 'x' markers denote simulations that were not possible to perform due to insufficient memory (for small number of cores), or not enough points to slab-decompose along z (for larger number of cores). See the caption of Fig. 7 for the description of the cases in the legend.

parallel performance of the algorithm, allowing for 2- to 8-fold speedups of the calculation, corresponding to a small wall-clock time per time step.

The numerical algorithm was implemented in a new DNS code, *SNaC*, which was made freely available and open-source. Given the flexibility and great performance of the tool, *SNaC* is expected to follow the footsteps of other research DNS codes such as *CaNS* and *AFiD*, and serve well as a base multi-block Navier-Stokes solver on top of which approaches for more complex phenomena can be implemented, such as a immersed-boundary methods for complex geometries [44, 45], numerical methods for two-phase [46, 47] or non-Newtonian flows [35].

In the near future, and in line with recent efforts in the fluid dynamics community, *SNaC* will be ported for massively parallel calculations on many Graphics Processing Units (GPUs) [48, 37, 49, 50]. In addition to this major

milestone, an in-house implementation of the multigrid solver will be sought which directly solves a batch of small linear systems, so that the inhomogeneity of the reduced 2D linear systems is fully covered without compromising the parallel performance.

Acknowledgements

I would like to thank Luca Brandt for interesting discussions, and the first users of *SNaC* from KTH Mechanics, Arash Banaei, Nazario Mastroianni, and Nicolò Scapin for the invaluable feedback and testing. Dr. Rob Falgout from Lawrence Livermore National Laboratory is thanked for suggesting the ‘sliced-pencils’ approach using *HYPRE* in Algorithm 2, as an alternative to Algorithm 3. Finally, Prof. Fernando Pinho from University of Porto (FEUP) is thanked for kindly providing the validation data from Ref. [41]. The computing time for the scaling tests was provided by the Swedish National Infrastructure for Computing (SNIC). This work was supported by the University of Iceland Recruitment Fund grant no. 1515-151341, *TURBBLY*.

References

- [1] TOP500, The List, top500.org, 2021. Accessed: 2021-05-01.
- [2] S. A. Orszag, G. Patterson Jr, Numerical simulation of three-dimensional homogeneous isotropic turbulence, *Physical Review Letters* 28 (1972) 76.
- [3] T. Ishihara, T. Gotoh, Y. Kaneda, Study of high-reynolds number isotropic turbulence by direct numerical simulation, *Annual Review of Fluid Mechanics* 41 (2009) 165–180.
- [4] S. Pirozzoli, J. Romero, M. Fatica, R. Verzicco, P. Orlandi, Reynolds number trends in turbulent pipe flow: a dns perspective, *arXiv preprint arXiv:2103.13383* (2021).
- [5] J. Kim, P. Moin, Application of a fractional-step method to incompressible navier-stokes equations, *Journal of computational physics* 59 (1985) 308–323.
- [6] R. Verzicco, P. Orlandi, A finite-difference scheme for three-dimensional incompressible flows in cylindrical coordinates, *Journal of Computational Physics* 123 (1996) 402–414.
- [7] A. Vreman, J. G. Kuerten, Comparison of direct numerical simulation databases of turbulent channel flow at $re \tau = 180$, *Physics of Fluids* 26 (2014) 015102.
- [8] P. Moin, R. Verzicco, On the suitability of second-order accurate discretizations for turbulent flow simulations, *European Journal of Mechanics-B/Fluids* 55 (2016) 242–245.
- [9] E. Fadlun, R. Verzicco, P. Orlandi, J. Mohd-Yusof, Combined immersed-boundary finite-difference methods for three-dimensional complex flow simulations, *Journal of computational physics* 161 (2000) 35–60.
- [10] W.-P. Breugem, B.-J. Boersma, Direct numerical simulations of turbulent flow over a permeable wall using a direct and a continuum approach, *Physics of fluids* 17 (2005) 025103.
- [11] M. Uhlmann, An immersed boundary method with direct forcing for the simulation of particulate flows, *Journal of Computational Physics* 209 (2005) 448–476.
- [12] G. Tryggvason, R. Scardovelli, S. Zaleski, *Direct numerical simulations of gas-liquid multiphase flows*, Cambridge University Press, 2011.
- [13] W. Aniszewski, T. Arrufat, M. Cialesi-Esposito, S. Dabiri, D. Fuster, Y. Ling, J. Lu, L. Malan, S. Pal, R. Scardovelli, et al., Parallel, robust, interface simulator (paris), *Computer Physics Communications* 263 (2021) 107849.
- [14] A. J. Chorin, Numerical solution of the navier-stokes equations, *Mathematics of computation* 22 (1968) 745–762.

- [15] G. H. Golub, C. F. Van Loan, *Matrix computations*, volume 3, JHU press, 2013.
- [16] P. N. Swarztrauber, The methods of cyclic reduction, fourier analysis and the facr algorithm for the discrete solution of poisson's equation on a rectangle, *Siam Review* 19 (1977) 490–501.
- [17] U. Schumann, R. A. Sweet, Fast fourier transforms for direct solution of poisson's equation with staggered boundary conditions, *Journal of Computational Physics* 75 (1988) 123–137.
- [18] P. N. Swarztrauber, R. A. Sweet, Vector and parallel methods for the direct solution of poisson's equation, *Journal of computational and applied mathematics* 27 (1989) 241–263.
- [19] P. Costa, A FFT-based finite-difference solver for massively-parallel direct numerical simulations of turbulent flows, *Computers & Mathematics with Applications* 76 (2018) 1853–1862.
- [20] R. Ostilla-Mónico, R. Verzicco, S. Grossmann, D. Lohse, The near-wall region of highly turbulent taylor–couette flow, *Journal of fluid mechanics* 788 (2016) 95–117.
- [21] P. Costa, F. Picano, L. Brandt, W.-P. Breugem, Universal scaling laws for dense particle suspensions in turbulent wall-bounded flows, *Physical Review Letters* 117 (2016) 134501.
- [22] M. S. Dodd, A. Ferrante, On the interaction of taylor length scale size droplets and isotropic turbulence, *Journal of Fluid Mechanics* 806 (2016) 356–412.
- [23] P. Cifani, J. Kuerten, B. Geurts, Highly scalable dns solver for turbulent bubble-laden channel flow, *Computers & Fluids* 172 (2018) 67–83.
- [24] E. P. Van Der Poel, R. Ostilla-Mónico, J. Donners, R. Verzicco, A pencil distributed finite difference code for strongly turbulent wall-bounded flows, *Computers & Fluids* 116 (2015) 10–16.
- [25] R. Borrell, O. Lehmkuhl, F. X. Trias, A. Oliva, Parallel direct poisson solver for discretisations with one fourier diagonalisable direction, *Journal of computational physics* 230 (2011) 4723–4741.
- [26] S. Laizet, N. Li, Incompact3d: A powerful tool to tackle turbulence problems with up to $o(10^5)$ computational cores, *International Journal for Numerical Methods in Fluids* 67 (2011) 1735–1757.
- [27] L. Santelli, P. Orlandi, R. Verzicco, A finite–difference scheme for three–dimensional incompressible flows in spherical coordinates, *Journal of Computational Physics* 424 (2021) 109848.
- [28] R. Mittal, G. Iaccarino, Immersed boundary methods, *Annu. Rev. Fluid Mech.* 37 (2005) 239–261.
- [29] R. D. Falgout, U. M. Yang, hypre: A library of high performance preconditioners, in: *International Conference on Computational Science*, Springer, 2002, pp. 632–641.
- [30] R. Verstappen, A. Veldman, Symmetry-preserving discretization of turbulent flow, *Journal of Computational Physics* 187 (2003) 343–368.
- [31] M. M. Rai, P. Moin, Direct simulations of turbulent flow using finite-difference schemes, *Journal of computational physics* 96 (1991) 15–53.
- [32] P. Wesseling, *Principles of computational fluid dynamics*, volume 29, Springer Science & Business Media, 2009.
- [33] D. W. Peaceman, H. H. Rachford, Jr, The numerical solution of parabolic and elliptic differential equations, *Journal of the Society for industrial and Applied Mathematics* 3 (1955) 28–41.
- [34] V. Fuka, Poissfft—a free parallel fast poisson solver, *Applied Mathematics and Computation* 267 (2015) 356–364.
- [35] Z. Ahmed, D. Izbassarov, P. Costa, M. Muradoglu, O. Tammisola, Turbulent bubbly channel flows: Effects of soluble surfactant and viscoelasticity, *Computers & Fluids* 212 (2020) 104717.
- [36] P. Orlandi, *Fluid flow phenomena: a numerical toolkit*, volume 55, Springer Science & Business Media, 2012.
- [37] P. Costa, E. Phillips, L. Brandt, M. Fatica, GPU acceleration of cans for massively-parallel direct numerical simulations of canonical fluid flows, *Computers & Mathematics with Applications* 81 (2021) 502–511.
- [38] XDMF Model and Format, xdmf.org, 2021. Accessed: 2021-05-01.
- [39] M. Frigo, S. G. Johnson, The design and implementation of fftw3, *Proceedings of the IEEE* 93 (2005) 216–231.
- [40] H. C. Ku, R. S. Hirsh, T. D. Taylor, A pseudospectral method for solution of the three-dimensional incompressible navier-stokes equations, *Journal of Computational Physics* 70 (1987) 439–462.
- [41] A. I. Miranda, P. J. Oliveira, F. Pinho, Steady and unsteady laminar flows of newtonian and generalized newtonian fluids in a planar t-junction,

- International journal for numerical methods in fluids 57 (2008) 295–328.
- [42] D. Liepsch, S. Moravec, A. Rastogi, N. Vlachos, Measurement and calculations of laminar flow in a ninety degree bifurcation, *Journal of biomechanics* 15 (1982) 473–485.
- [43] A. Chiarini, M. Quadrio, The turbulent flow over the barc rectangular cylinder: a dns study, *Flow, Turbulence and Combustion* (2021) 1–25.
- [44] F. Dalla Barba, F. Picano, A novel approach for direct numerical simulation of hydraulic fracture problems, *Flow, Turbulence and Combustion* 105 (2020) 335–357.
- [45] P. Berghout, X. Zhu, D. Chung, R. Verzicco, R. J. Stevens, D. Lohse, Direct numerical simulations of taylor–couette turbulence: the effects of sand grain roughness, *Journal of fluid mechanics* 873 (2019) 260–286.
- [46] N. Scapin, P. Costa, L. Brandt, A volume-of-fluid method for interface-resolved simulations of phase-changing two-fluid flows, *Journal of Computational Physics* 407 (2020) 109251.
- [47] H.-R. Liu, C. S. Ng, K. L. Chong, D. Lohse, R. Verzicco, An efficient phase-field method for turbulent multiphase flows, *arXiv preprint arXiv:2105.01865* (2021).
- [48] X. Zhu, E. Phillips, V. Spandan, J. Donners, G. Ruetsch, J. Romero, R. Ostilla-Mónico, Y. Yang, D. Lohse, R. Verzicco, et al., Afid-gpu: a versatile navier–stokes solver for wall-bounded turbulent flows on gpu clusters, *Computer physics communications* 229 (2018) 199–210.
- [49] M. Bernardini, D. Modesti, F. Salvatore, S. Pirozzoli, Streams: A high-fidelity accelerated solver for direct numerical simulation of compressible turbulent flows, *Computer Physics Communications* 263 (2021) 107906.
- [50] S. Ha, J. Park, D. You, A multi-gpu method for adi-based fractional-step integration of incompressible navier-stokes equations, *Computer Physics Communications* 265 (2021) 107999.

Appendix A. Alternative approach for solving the Poisson equation

Here we present an alternative approach that may be employed for the solution of n , 2D linear systems (Eq. 9), using a slab domain decomposition. Unlike Algorithm 2, where an appropriate value of p needs to be determined, this approach does not require tuning. Let $\underline{n}^b = [n_1^b, n_2, n_3^b]$ be the number of grid points in each direction specific to block b , with the same number of grid points in the synthesis direction (here taken again as x_2 , so $n_2^b = n_2$). Instead of solving the 2D linear systems sequentially in a pencil domain decomposition, we follow the FFT-based synthesis by a *redistribution* of the domain decomposition within each block to a *slab-like* configuration, as illustrated in the right drawing of Fig. A.10.

In this configuration, each subdomain m has a size $[n_1^b, n_2^m, n_3^b]$, i.e., with the points along x_2 decomposed by the total number of tasks within block b . This operation is employed using an *all-to-all*⁴ collective operation within the group of tasks of each block (i.e., under `comm_block`). Solving the iterative system using this configuration has clear advantages: first, the communication required for each 2D system much smaller; second, the solution of the different n_2 systems is now *parallel*, in batches of size n_2^m . We will see that these advantages justify the overhead of the *all-to-all* collective, especially if n_2 is large enough. Besides the collective operations, a downside of this approach is the hard limit of the number of tasks per block, which cannot exceed n_2 in this example. However, this restriction can be significantly relaxed by leveraging shared-memory parallelization.

As Fig. A.10 illustrates, the slab decomposition is not required to be congruent among the different blocks –

⁴In practice, implemented using `MPI_ALLTOALLW` and `MPI_TYPE_SUBARRAY` derived types.

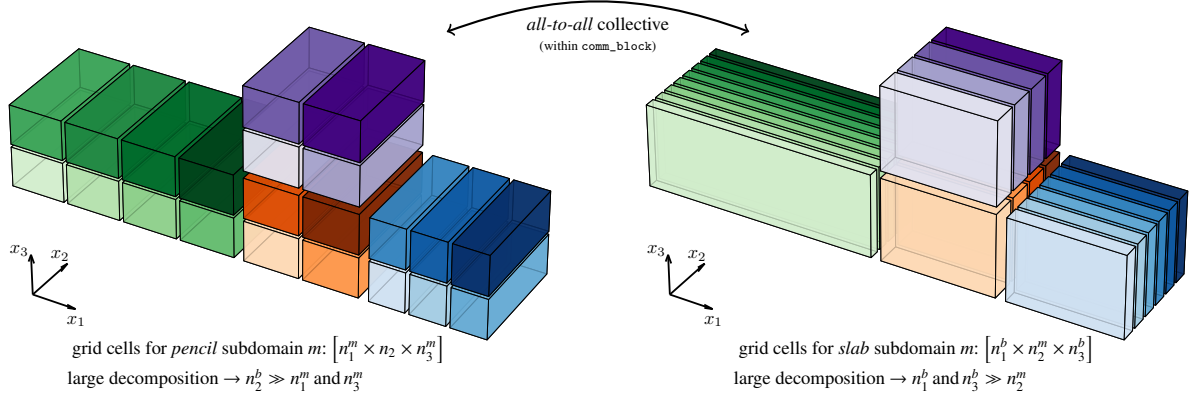


Figure A.10: Illustration of two different domain decompositions which may be used to solve the FFT-accelerated Poisson equation, assuming x_2 as the FFT synthesis direction. Different colors distinguish the tasks in different blocks, while different lightness marks the MPI tasks within a block. The left side shows a pencil decomposition, required for the FFT-based synthesis, and the right side shows a slab decomposition within each block used for the solution of Eq. (9). The redistribution from one distribution to the other requires a collective *all-to-all* operation, performed within the group of ranks within each block (`comm_block`).

domains with larger values of $n_1^b \times n_3^b$ can be more decomposed, to ensure load balancing. This means that the communicator associated with the iterative solution of the n_2^m 2D systems to be passed to *HYPRE* cannot be `comm_block`. Instead, an array of MPI communicators `comm_slab(:)` is determined, where each element encapsulates the tasks in charge of the 2D linear system associated with the plane with index j . The overall approach for the parallel FFT-based solution of the Poisson equation is presented in Algorithm 3.

Algorithm 3 Sequence of operations performed per task for the parallel solution of the Poisson equation (Eq. (8)) with FFT-based synthesis, using a pencil \leftrightarrow slab data redistribution.

```

do  $i = 1$  to  $n_1^m$  and  $k = 1$  to  $n_3^m$ 
  forward FFT-based transform along  $x_2$  of right-hand-side of Eq. (8):  $\hat{f}_{i,1\dots n_2,k} = \mathcal{F}_{x_2}(f_{i,1\dots n_2,k})$ 
end do
pencil $\rightarrow$ slab redistribution within each block (i.e., within comm_block) to obtain  $\hat{f}_{1\dots n_1^b,1\dots n_2^m,1\dots n_3^b}$ 
do  $j = 1$  to  $n_2^m$ 
  solve Eq. (9) within comm_slab(j) using a geometric multigrid solver to obtain  $\hat{\Phi}_{1\dots n_1^b,j,1\dots n_3^b}$ 
end do
slab $\rightarrow$ pencil redistribution within each block (i.e., within comm_block) to obtain  $\hat{\Phi}_{1\dots n_1^m,1\dots n_2,1\dots n_3^m}$ 
do  $i = 1$  to  $n_1^m$  and  $k = 1$  to  $n_3^m$ 
  backward FFT-based transform along  $x_2$  of the solution:  $\Phi_{i,1\dots n_2,k} = \mathcal{F}_{x_2}^{-1}(\hat{\Phi}_{i,1\dots n_2,k})$ 
end do

```
